

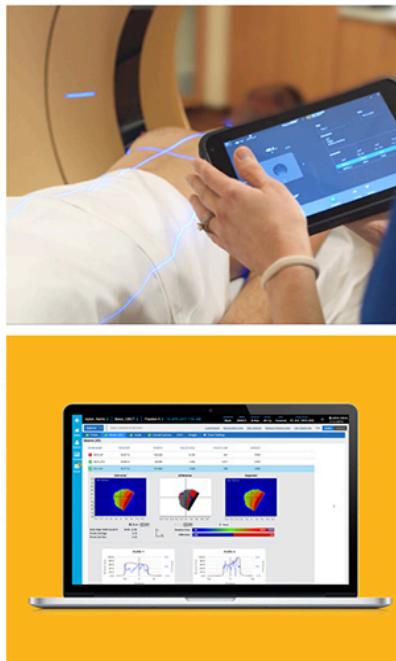
Patient Safety Starts with **Independence.**

With ever-increasing imaging and treatment variables, an independent approach to Quality Management ensures safety is never taken for granted.

At Sun Nuclear, we deliver proven independent QA solutions for Radiation Therapy and Diagnostic Imaging. More than 5,000 hospitals and clinics worldwide count on us to help:

- Mitigate errors
- Reduce inefficiencies
- Validate technologies and techniques
- Elevate clinical care

For user insights, key publications and product updates, visit **sunnuclear.com**.



Model-based measurements of the diameter of the internal carotid artery in CT angiography images

H. A. F. Gratama van Andel^{a)}

Department of Biomedical Engineering and Physics, Academic Medical Center, P. O. Box 22600, 1100 DD Amsterdam, The Netherlands

H. W. Venema

Department of Biomedical Engineering and Physics, Academic Medical Center, P. O. Box 22600, 1100 DD Amsterdam, The Netherlands and Department of Radiology, Academic Medical Center, P. O. Box 22600, 1100 DD Amsterdam, The Netherlands

K. Bol

Department of Medical Informatics, Erasmus MC, P. O. Box 2040, 3000 CA Rotterdam, The Netherlands

H. A. Marquering

Department of Biomedical Engineering and Physics, Academic Medical Center, P. O. Box 22600, 1100 DD Amsterdam, The Netherlands and Department of Radiology, Academic Medical Center, P. O. Box 22600, 1100 DD Amsterdam, The Netherlands

C. B. Majoie and G. J. den Heeten

Department of Radiology, Academic Medical Center, P. O. Box 22600, 1100 DD Amsterdam, The Netherlands

C. A. Grimbergen

Department of Biomedical Engineering and Physics, Academic Medical Center, P. O. Box 22600, 1100 DD Amsterdam, The Netherlands

G. J. Streekstra

Department of Biomedical Engineering and Physics, Academic Medical Center, P. O. Box 22600, 1100 DD Amsterdam, The Netherlands and Department of Radiology, Academic Medical Center, P. O. Box 22600, 1100 DD Amsterdam, The Netherlands

(Received 23 September 2009; revised 28 August 2010; accepted for publication 2 September 2010; published 12 October 2010)

Purpose: Computed tomography angiography (CTA) is often used to determine the degree of stenosis in patients that suffer from carotid artery occlusive disease. Accurate and precise measurements of the diameter of the stenosed internal carotid artery are required to make decisions on treatment of the patient. However, the inherent blurring of images hampers a straightforward measurement, especially for smaller vessels. The authors propose a model-based approach to perform diameter measurements in which explicit allowance is made for the blurring of structures in the images. Three features of the authors' approach are the use of prior knowledge in the fitting of the model at the site of the stenosis, the applicability to vessels both with circular and noncircular cross-section, and the ability to deal with additional structures close to the arteries such as calcifications.

Methods: Noncircular cross-sections of vessels were modeled with elliptic Fourier descriptors. When calcifications or other high-intensity structures are adjacent to the lumen, both the lumen and the high-intensity structures were modeled in order to improve the diameter estimates of the vessel. Measurements were performed in CT scans of a phantom mimicking stenosed carotids and in CTA scans of two patients with an internal carotid stenosis. In an attempt to validate the measurements in CTA images, measurements were also performed in three-dimensional rotational angiography (3DRA) images of the same patients.

Results: The validity of the approach for diameter measurements of cylindrical arteries in CTA images is evident from phantom measurements. When prior knowledge about the enhancement and the blurring parameter was used, accurate and precise diameter estimates were obtained down to a diameter of 0.4 mm. The potential of the presented approach, both with respect to the extension to noncircular cross-sections and the modeling of adjacent calcifications, appears from the patient data. The accuracy of the size estimates in the patient images could not be unambiguously established because no gold standard was available and the quality of the 3DRA images was often suboptimal.

Conclusions: The authors have shown that the inclusion of *a priori* information results in accurate and precise diameter measurements of arteries with a small diameter. Furthermore, in patient data,

the assumption of a circular cross-section often appears to be too simple. The extension to noncircular cross-sections and adjacent calcifications paves the way to realistic modeling of the carotid artery. © 2010 American Association of Physicists in Medicine. [DOI: [10.1118/1.3491808](https://doi.org/10.1118/1.3491808)]

Key words: blood vessels, head & neck, computerized tomography, diagnostic radiography, image registration, medical image processing, vessel segmentation, elliptic Fourier descriptor, carotid stenosis, CT angiography

I. INTRODUCTION

Stenosis of the internal carotid artery may lead to neurological symptoms and is considered to be the major risk factor for ischemic stroke. Whether a patient will benefit from treatment, endarterectomy, or endovascular stent placement depends on the severity of the stenosis.^{1–4} Digital subtraction angiography has historically been the gold standard to assess the severity of stenosis, but it has been shown that it can be replaced by the less invasive three-dimensional techniques magnetic resonance angiography and computed tomography angiography (CTA).^{5,6} CTA is often used for the quantification of carotid stenosis as it is relatively cheap and widely available.^{7,8}

As manual measurements give rise to interobserver and intraobserver variations, there has been an interest in automated methods in stenosis quantification in CTA. Methods described in the literature encounter various complications: They show a decreasing accuracy and precision in size measurements of smaller vessels,^{9,10} are influenced by the convolution kernel used for the reconstructed images,¹⁰ are dependent on the amount of contrast enhancement,¹¹ and tend to have problems with the presence of calcifications.^{12,13}

Underlying these problems is the blurring of the images, which is inherent in CT imaging. This blurring, which can be modeled by the convolution of the vessel geometry with a point-spread function (PSF), causes conventional methods^{14,15} to inaccurately locate the vessel boundary, leading to a bias in size estimates.¹⁶ Adequate dealing with this bias in measurements of the vessel size at the site of a stenosis is obviously of crucial importance for quantification of the stenosis.

Various approaches have been introduced to overcome this problem, each, however, with its own limitations. One method tries to reduce the average bias by the use of training datasets and specific imaging protocols.¹⁷ This, however, limits applicability and results in reduced accuracy for small vessels as the bias depends on the diameter. Other methods^{18,19} use special unbiased edge detectors using image derivatives. This procedure may be difficult or unreliable at the site of a stenosis as the signal-to-noise ratio (SNR) is low at that site. To reduce the SNR problem, the full-width at half-maximum (FWHM) criterion has been used, which is more robust in the presence of noise than the derivative-based edge detectors. The bias of the FWHM criterion can be corrected if the PSF of the imaging system is known and cylindrical vessels are assumed.²⁰ However, obtaining FWHM values from the image data may be unreliable in vessels of only a few pixels in diameter.

Another option is a model-based approach, in which explicit allowance is made for the blurring of the image. In principle, this eliminates the bias in the diameter measurements. The fitting of a parametric model for size measurements has proved to be useful in projection images^{21–23} and in three-dimensional data.^{24,25} Wörz *et al.*^{24,26,27} describe a model-based approach for vessel segmentation and quantification in which a vessel is modeled as a cylindrical tubular structure in a homogeneous background. However, vessels often are *not* cylindrical. Another complication is that calcifications may be present in the vessel wall or other high-intensity structures may be nearby, which affects the assumption of the homogeneity of the background.

In this paper, we propose a more extensive model-based approach for stenosis measurements in CTA images. In its basic form, a parametric image of a blurred circular disk-shaped cross-section of a cylinder is fitted to the cross-sectional image of a vessel. The extended model allows for both noncylindrical vessel shapes and the presence of calcifications or other high-intensity structures nearby. The extension to more general shapes is obtained by the use of elliptic Fourier descriptors for the shape of the cross-section of the vessel.^{28–30} When calcifications or other high-intensity structures are present, both the lumen of the vessel and the high-intensity structures are modeled to improve the estimates of the size of the vessel. In this study, the size of noncircular lumen cross-sections is characterized with the *equivalent diameter*, which is the diameter of a circle with an area equal to the area of the lumen cross-section. For circular cross-sections, the equivalent diameter thus equals the conventional diameter.

In model-based approaches of (equivalent) diameter measurements, a considerable number of parameters have to be estimated. At sites of low SNR this may result in fits with poor precision. For small diameters, the estimation procedure may be ill-defined because of a dependency of the parameters and as a consequence, additional information is needed to obtain reliable estimates.^{26,27} Three important parameters are the intensity of lumen and background and the width of the PSF. In CTA, the intensity of an artery is variable over different patients and scan protocols^{31,32} and the width of the PSF depends on the type of scanner and reconstruction filter. However, it has been shown that within one patient, the contrast between the artery and surrounding tissue for the distal common carotid artery and the internal carotid artery varies less than 10%.^{31–33} In a limited volume of interest of a single CTA scan, the width of the PSF may be assumed to be constant. The constancy of the intensity of the background often is also a reasonable assumption. Consequently, it can be ex-

pected that estimates of these three parameters from images in which the lumen area of the artery is large are sufficiently accurate to be used as reliable prior information in the parameter estimation in images at the stenosed site. In the present paper, the consequences of the use of prior knowledge of these three parameters are investigated for the accuracy and precision of diameter measurements.

Measurements were performed in phantom images and in CTA scans of patients with an internal carotid stenosis. In an attempt to validate the equivalent diameter estimates in the clinical images, two patients were selected for which the equivalent diameters could be measured in three-dimensional rotational angiography (3DRA) images as well. In 3DRA, the contrast of the arteries is greatly enhanced because the contrast is administered intra-arterial instead of intravenously, as is the case in CTA. Therefore, these images have a higher SNR than CTA images.^{34–36} Furthermore, calcifications are hardly visible in these images, thus eliminating one of the problems present in CTA.

II. MODELING OF BLOOD VESSELS AND THEIR SURROUNDINGS IN CTA IMAGES

We assume a CT scanner to be a linear imaging system. In the absence of noise, the image intensity $I(x, y, z)$ of a three-dimensional (3D) attenuation coefficient distribution $\mu(x, y, z)$ can be described by the convolution of $\mu(x, y, z)$ with the 3D PSF $h(x, y, z)$

$$I(x, y, z) = \mu(x, y, z) * h(x, y, z). \quad (1)$$

Strictly speaking, the PSF of a CT scanner is dependent on the position in the image. However, in a limited size of the region of interest (ROI), it is reasonable to assume the PSF to be shift invariant. For the relatively smooth kernels that are used in the reconstruction of CTA images, the PSF can be approximated with a 3D Gaussian function,³⁷ i.e.,

$$h(x, y, z, \sigma_{xy}, \sigma_z) = \frac{1}{2\pi\sigma_{xy}^2} e^{-(x^2+y^2)/2\sigma_{xy}^2} \frac{1}{\sqrt{2\pi}\sigma_z} e^{-z^2/2\sigma_z^2}. \quad (2)$$

In Eq. (2), σ_{xy} and σ_z characterize the in-plane and the out-of-plane sharpness, respectively.

In CTA images, blood vessels are enhanced due to the presence of contrast agent in the blood that has been administered intravenously to the patient. We consider an artery that is orthogonal to the xy -plane, with an (equivalent) diameter that changes relatively slowly in the z -direction. For the part of the internal carotid artery considered in this study, the first assumption is reasonable. The second condition is not always fulfilled, for instance, when calcifications are present. We will return to the limitations in the discussion.

II.A. Tubular model

An artery is modeled by a straight tube oriented in the z -direction. The cross-section is circular, with a radius $R(z)$, and the tube is filled with contrast enhanced blood. We assume that the tube is surrounded by homogeneous tissue. The 3D image of this model is blurred by the PSF of the imaging

system, which in this study is approximated with a 3D Gaussian function with parameters σ_{xy} in the xy -plane and σ_z in the z -direction [Eq. (2)].

It can be shown (Appendix A) that the intensity of the 3D model image as a function of the distance r from the center of the tube is given by

$$I(r, z) = I_b + (I_f - I_b) e^{-r^2/2\sigma_{xy}^2} \sum_{k=0}^{\infty} \frac{1}{k!^2} \left(\frac{r^2}{2\sigma_{xy}^2} \right)^k \times \left(k! - \Gamma\left(1 + k, \frac{R(z)^2}{2\sigma_{xy}^2}\right) \right), \quad (3)$$

with I_f and I_b as the intensity of the lumen of the artery and the background, respectively. In practice the summation is truncated at an upper limit k_{\max} that is chosen to obtain an approximation of $I(r, z)$ within the machine precision.

Because we assume that the diameter in the z -direction varies slowly, we only need to consider 2D images. A cross-sectional image at $z=z_0$ consists of a circular disk with radius $R(z_0)$ and intensity I_f in a background with intensity I_b , blurred by a 2D Gaussian with parameter σ_{xy} . A 2D model image can therefore be described by six parameters: The coordinates of the center of the disk (x_0, y_0), $R(z_0)$, I_f , I_b , and σ_{xy} . For notational convenience, the dependency of I and R on z is not indicated in the remainder of this article and σ is used instead of σ_{xy} .

II.B. Extended model

For the modeling of vessels and their immediate surroundings, the tubular model may be an unacceptable simplification because (1) arteries often have a noncircular cross-section, especially when they are diseased, and (2) in the immediate surroundings of the artery high-intensity structures, such as calcifications, may be present. Therefore, the basic tubular model of Sec. II A is extended for use in clinical images to include (1) arteries with noncircular cross-sections and (2) structures in the background with deviant intensity. The intensities within the artery, background structures, and remaining background are assumed to be constant.

As in the tubular model, the cross-sections of the arteries and background structures are assumed to change slowly in the z -direction. Consequently, in the 2D images only blurring in the xy -plane has to be considered.

In an unblurred 2D model image ($\sigma=0$) the contours of both the arteries and background structures are described using elliptic Fourier descriptors (EFDs).^{28–30}

In this representation, each contour, parametrized by $0 \leq t < 2\pi$, is expressed as

$$\begin{bmatrix} x(t) \\ y(t) \end{bmatrix} = \begin{bmatrix} x_0 \\ y_0 \end{bmatrix} + \sum_{k=1}^N \begin{bmatrix} a_k & b_k \\ c_k & d_k \end{bmatrix} \begin{bmatrix} \cos kt \\ \sin kt \end{bmatrix}, \quad (4)$$

with (x_0, y_0) the center of the contour, N the number of Fourier terms, and $(a_k, b_k, c_k, d_k, k=1, N)$ the Fourier parameters.²⁹ For $N=1$, the contour is an ellipse and for $N > 1$, the contour can be viewed as being decomposed into a

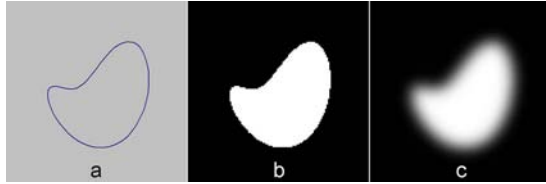


FIG. 1. Example of calculation of 2D model image with one shape. (a) shows a contour that was generated using Eq. (4) with $N=2$ Fourier terms. In (b), all pixels with centers within the contour were given the intensity I_f ; the other pixels intensity I_b . (c) was obtained by blurring image (b) with a 2D Gaussian with $\sigma=5$ pixels. Each image measures 128×128 pixels.

sum of rotating phasors, each defining an ellipse and rotating with a speed proportional to their harmonic number k .²⁹

Each unblurred shape of a 2D extended model image, describing the cross-section of the carotid or of an adjoining high-intensity structure, is described by $3+4N$ parameters x_0 , y_0 , I_f , and $(a_k, b_k, c_k, d_k, k=1, N)$. Each model image has two additional parameters: I_b and σ .

II.C. 2D model images and parameter estimation

Cross-sectional images of the tubular model (Sec. II A) were determined by calculating for each pixel position (x, y) the intensity $I(r)$ according to Eq. (3).

No closed-form solution for the calculation of 2D model images of the extended model (Sec. II B) is available. These images were calculated in the following way. First, the pixels with centers within the contour that bounds each (unblurred) shape were given the intensity I_f of the shape and the intensity of the remaining pixels was set to I_b . Next, the image was blurred by convolution with a Gaussian kernel with parameter σ (see Fig. 1).

To estimate the parameters of an image $I_{\text{im}}(\mathbf{x})$ containing the artery and its surroundings, with \mathbf{x} the vector of pixel positions within a ROI, a model image $I(\mathbf{x}, \mathbf{p})$, with \mathbf{p} the parameter vector, was fitted by minimizing the root-mean-square (RMS) objective function

$$\text{RMS} = \sqrt{\sum (I_{\text{im}}(\mathbf{x}) - I(\mathbf{x}, \mathbf{p}))^2}. \quad (5)$$

Minimization of Eq. (5) was performed with the downhill simplex method. The size of the lumen cross-section is characterized with the equivalent diameter of the lumen. For the extended model, the equivalent diameter equals $2\sqrt{A/\pi}$, with A the area of the lumen cross-section. For the tubular model, the equivalent diameter equals the conventional diameter.

II.D. Use of prior knowledge

In the fitting process described above, the complete parameter vector \mathbf{p} can be estimated, but it is also possible to use *prior knowledge* for three parameters: The arterial intensity I_f , the background intensity I_b , and the blurring parameter σ . When the diameter of the artery is very small, the use of prior knowledge is indispensable. In this case only the product of intensity and cross-sectional area can be determined and not both quantities separately.²⁷ For CTA examinations, the arterial intensity I_f can be assumed to be reason-

ably constant within the relative small volume of the carotid artery that is analyzed because of the venous injection of the contrast agent, the mixing of contrast and blood between the site of injection and the site of the scan, and the short scan time. Also, the constancy of the intensity of the background I_b is often a reasonable assumption. The value of σ depends on the scanner, the scanning protocol, and the reconstruction kernel, but is constant within one examination.

In our approach, the complete parameter vector was estimated in a part of the carotid artery with a large diameter, and thus with a high SNR. Estimates of I_f , I_b , and σ from this set were used as prior knowledge in modeling cross-sectional images at the site of a stenosis, where the SNR is lower. The variation in background intensity I_b may not always be negligible, however. Therefore also fits were made using only prior knowledge of I_f and σ .

III. DATA ACQUISITION AND PREPROCESSING

III.A. CT scans

A 64-slice CT scanner (Brilliance 64, Philips Healthcare, Best, The Netherlands) with a collimation of 64×0.625 mm was used. Spiral scans were made using a rotation time of 0.75 s, high resolution, pitch of 0.765, 120 kV, and 265 effective mAs. Images were reconstructed on a 512×512 matrix with a field of view (FOV) of 150 mm, resulting in a pixel size of 0.3×0.3 mm², a nominal slice width of 0.9 mm, a slice increment of 0.45 mm, and reconstruction kernel B (smooth).

III.B. Phantoms

The accuracy and precision of the diameter measurements using the tubular model was investigated with two phantoms mimicking the neck, each one with four arteries near the center. The phantoms were made of nylon and consisted of a cylinder with a diameter of 110 mm and a length of 100 mm. The two phantoms contained a number of cylindrical holes, each one with a length of 45 mm, 15 mm from the center of the phantom. The first phantom contained four holes with diameters of 6.0 mm and four smaller holes with diameters of 4.2, 2.4, 1.2, and 0.6 mm; in the second phantom, the diameter of the four larger holes was 4.0 mm and of the smaller holes 2.8, 1.6, 0.8, and 0.4 mm (see Fig. 2). The 6 and 4 mm holes were chosen to mimic healthy internal carotids and the smaller holes mimicked stenosed segments of different stenosis degree. The 4.2 mm “smaller” hole in the first phantom was not used in the measurements. The segments containing the three smallest holes (0.4, 0.6, and 0.8 mm) consisted of a stack of small cylinders, each with a height of 1 cm [in Fig. 2(e), partitions are faintly visible, for instance, in the cylinder containing the 0.8 mm hole]. This setup was chosen in order to facilitate the drilling of these holes.

The holes were filled with a water diluted contrast agent (Visipaque 320 mg I/ml, 1:24). This concentration was cho-

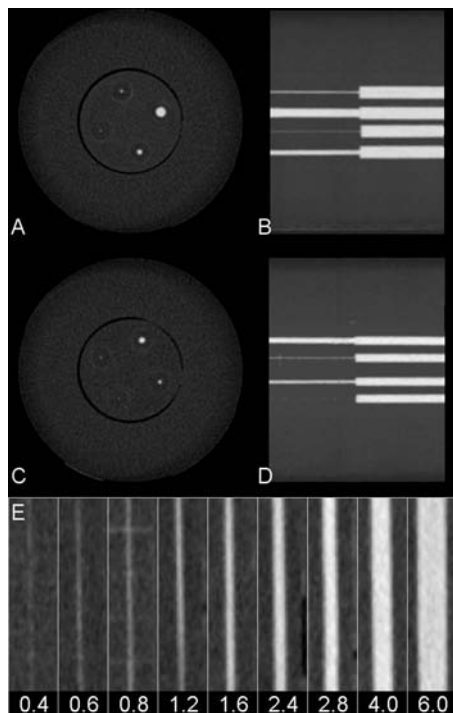


FIG. 2. [(a)–(d)] The two phantoms mimicking the neck with four arteries near the center. [(a) and (c)] Axial images of phantoms 1 and 2 with holes with diameters of 4.2, 2.4, 1.2, and 0.6 mm and 2.8, 1.6, 0.8, and 0.4 mm, respectively. The holes are filled with a water diluted contrast agent. [(b) and (d)] Maximum intensity projections at the sagittal plane of both phantoms, showing at the left the holes with diameters between (b) 4.2 and 0.6 mm and (d) 2.8 and 0.4 mm, and at the right the reference holes of (b) 6.0 and (d) 4.0 mm. The smallest holes are nearly invisible. (e) A composition of sagittal images through the center of the holes with sizes used in this study. The 4.2 mm hole was not used. The window center is 200 HU; the window width is 400 HU.

sen to obtain an intensity of 350 HU, a value comparable to that in a typical clinical scan. A scan as made of each phantom with its axis aligned in the z -direction.

The diameter of the circular cross-section of each cylindrical hole was estimated in approximately 40 axial images, 1 mm apart.

III.C. PSF measurements

The value of the σ of the PSF was also determined in a conventional way: A scan was made of a small block of polyvinyl chloride (PVC) of approximately $3 \times 4 \times 4$ cm³, with a CT value of approximately 1100 HU. It was scanned in a small water-filled PMMA cylinder (outer diameter 70 mm) and CT images were acquired using the acquisition and reconstruction parameters listed in Sec. III A. In both the x - and y -directions, five images of 80×50 pixels containing the edge of the cube were used to estimate σ by fitting a convolution of a Gaussian and a step edge to the image data.

III.D. Patients

III.D.1. CTA images

To test the feasibility of our approach in clinical data we performed size measurements of the cross-section of the in-

ternal carotid artery in CTA images of two patients. For these two patients, 3DRA images were also available (see below). Patient 1 was scanned on the 64-slice scanner, patient 2 was scanned on a four-slice CT scanner (Mx8000 Quad, Philips Healthcare, Best, The Netherlands). The acquisition and reconstruction parameters of the 64-slice scanner are listed in Sec. III A. For the four-slice scanner, the same acquisition parameters were used, apart from a collimation of 4×1 mm and a pitch of 0.875. For this scanner, the nominal slice width was 1.3 mm and the slice increment 0.5 mm.

On the 64-slice scanner, the patient was scanned from just below the aortic arch to just above the circle of Willis and 80 ml contrast agent (Visipaque 320 mg I/ml) was injected at a rate of 4 ml/s. On the four-slice scanner, the patient was scanned from just above the shoulders to just above the circle of Willis and 120 ml contrast agent was injected. For both scanners, the scanning delay was automatically adjusted by a bolus-tracking technique.

III.D.2. 3DRA images

3DRA examinations were performed on a single-plane angiographic unit (Integris Allura Neuro; Philips Healthcare, Best, The Netherlands) using propeller rotation.³⁸ While 15–21 ml contrast agent (Visipaque 320 mg I/ml) at 3 ml/s was injected through a 6F catheter positioned in the common carotid artery, 100 projection images were acquired during a 240° rotational run in 8 s. Images were reconstructed on a 256×256 matrix, with a FOV of 70 mm and a slice increment of 0.27 mm.

III.D.3. Registration of CTA and 3DRA images

To spatially relate the CTA and 3DRA size measurements, the external and internal carotid artery were segmented. This segmentation was used for registration of the two modalities and was performed with open source software available in the Vascular Modeling Toolkit.³⁹ An initial segmentation was performed by placing seed points in all the vessels of interest and applying a colliding fronts method^{40,41} using a lower threshold of 150 HU and an upper threshold of 400 HU in CTA. For 3DRA images, only a lower threshold was used with a value halfway between the average background value and the average lumen intensity. Next, a segmentation was performed using a geodesic level set segmentation method based on the image gradients.⁴² In the case of CTA images, a correction was included for the presence of high-intensity structures as bone and calcifications (defined with a lower threshold of 450 HU).⁴³ The surfaces of the segmented arteries in the 3DRA images and CTA images were registered using an iterative closest point registration.⁴⁴ In the CTA images, a centerline was determined through the segmented internal carotid artery based on solving the Eikonal equation on a Voronoi diagram.⁴⁰ Cross-sectional images perpendicular on this centerline were made of the internal carotid artery from both CTA and 3DRA using cubic interpolation with a pixel size of 0.1 mm, an image size of 128^2 pixels centered on the artery, and an increment of 0.1 mm.

III.D.4. Selection of CTA and 3DRA images

For each patient, the segment containing the stenosis was selected within the CTA and 3DRA scans and two reference segments, one proximal and the other distal to the stenosis. The reference segments were chosen in order to obtain estimates of the parameters I_f , I_b , and σ , to be used as prior knowledge in the estimation of the equivalent diameter in the stenosed segment. Two reference segments were chosen in order to have a check on the invariance of these parameters along the vessel. The first reference segment was in the common carotid close to the bifurcation and the second reference segment was in the internal carotid a few cm distal to the site of stenosis. The segments have a length of 6–10 mm, and in a segment, 12–20 images were analyzed.

IV. FITTING OF 2D MODEL IMAGES—PRACTICAL ASPECTS

The parameters of an image $I_{\text{im}}(x)$ were obtained by fitting a model image $I(x, p)$ by minimizing the objective function [Eq. (5)] using the downhill simplex method.^{45,46} In this method, initial estimates for the parameters p_{ini} have to be specified, as well as step sizes dp to indicate the expected deviation of initial and optimal value for each parameter.

The fitting procedure of the 2D images consists of a number of steps:

- (1) Segmentation of the image, in order to obtain a first approximation of the carotid artery, and other shapes, if present;
- (2) Definition of the ROI containing the approximation of the carotid artery and a border region;
- (3) Choice of the number of Fourier terms for each shape, choice of the use of prior knowledge for parameters I_f , I_b , and σ , or not, and calculation of the initial parameter values p_{ini} ;
- (4) Choice of initial step sizes dp ;
- (5) Calculation of model images and minimization of objective function [Eq. (5)].

IV.A. Phantom data; tubular model

IV.A.1. Segmentation and definition ROI

For each cylindrical hole cross-section, subimages were created of 64×64 pixels with the center of the lumen in the center of the image. In these subimages, circular ROIs with a diameter of 8 mm were used around the center of each lumen. Identification of the lumen was performed in the following way.

Within each ROI, the maximal intensity was determined. The background intensity was defined as the average value of a ring 2 pixels wide at the border of the ROI. A segmentation of vessel and background was obtained by thresholding the image with the average of these two intensities. In case more than one connected region was present within the ROI after thresholding, a situation that sometimes occurred with small cylinders with low contrast due to the presence of

TABLE I. The initial step sizes used in the simplex minimization method.

Parameter p	Step size dp
x_0, y_0	0.4 mm
R	0.2 mm
σ	0.1 mm
I_f	50 HU
I_b	25 HU

noise, the connected region closest to the center of the ROI was considered to be the cylinder cross-section.

IV.A.2. Initialization of p and dp

The coordinates of the center of gravity of the segmented cylinder cross-section were taken as initial values for (x_0, y_0) . The equivalent radius $(\sqrt{S/\pi})$, with S the area of the cross-section, was used as initial value for R . The mean values of the intensity of structure representing the cylinder cross-section and background were used as initial value of I_f and I_b . A default value of 0.5 mm was used as initial value of σ .

This procedure did not provide reliable initial values of R and I_f for very small cylinders. For the 0.8, 0.6, and 0.4 mm cylinders, a different initialization for R was used (Appendix B). I_f was initialized with $I_b + 300$ as the contrast in the phantom between cylinder and surrounding was roughly 300 HU. The exact choice of the contrast value was not critical. After some experimentation, it appeared that the initial step sizes dp listed in Table I were adequate.

The diameters of all cylinders were estimated using all six parameters of the tubular model. For cylinders with a diameter smaller than 4 mm, model fitting was also performed using prior knowledge for three of the six parameters (I_f , I_b , and σ), using the mean estimates of the fitted 6 mm cylinder (for the 2.4, 1.2, and 0.6 mm cylinders) or 4 mm cylinder (for the 2.8, 1.6, 0.8, and 0.4 mm cylinders).

IV.A.3. Calculation of model images and minimization of objective function

Model images were calculated using Eq. (3) of the tubular model. In the simplex algorithm, a maximum of 500 iterations was chosen. Once a minimum is found, it is customary to restart the procedure at least once. Parameter values for which the minimum error was obtained were used as initial values and a check was made whether in the second run the same minimum was found.⁴⁶ When this was not the case, we continued with restarts until in successive runs the same minimum was obtained.

In order to judge the performance of the model-based approach presented here in comparison to conventional methods without bias-correction, we also calculated the expected diameters according to the FWHM criterion and using the second order derivative zero-crossing.²⁵ These calculations were performed numerically using Eq. (3).

TABLE II. The thresholds used in the segmentation to obtain initial contours for the extended model in the patient data.

Reference segment		Stenotic segment
<i>CTA images</i>		
High threshold	250 HU	Average value of 4×4 central pixels
Low threshold	150 HU	150 HU
<i>3DRA images</i>		
High threshold	$I_{bgr} + 0.75(I_{fgr} - I_{bgr})$	Average value of 4×4 central pixels
Low threshold	$I_{bgr} + 0.5(I_{fgr} - I_{bgr})$	$I_{bgr} + 0.5(I_{fgr} - I_{bgr})$

IV.B. Patient data; extended model

IV.B.1. Segmentation

For all images except those of the stenotic segment of patient 1 that contained calcifications, the following procedure was used.

Initial segmentation of the carotid artery and of peripheral structures, if present, was performed by thresholding. The use of one single threshold value did not always provide satisfactory results, as sometimes the central artery and a structure nearby remained connected or the central artery could be missed. Therefore, segmentation was performed using two thresholds, a high one and a low one (Table II). With the high threshold, part of the central artery was found and, unconnected with the central artery, part of high-intensity structure(s) nearby, if present. With the low threshold, *all* structures were identified that had to be modeled. All structures within the high thresholded image were dilated, one pixel at a time, conditionally on the presence of pixels in the low thresholded image and not allowing overlap. In this way, the segmented central artery and segmented high-intensity structures nearby remained separated. Finally, the remaining structures of the low thresholded image were added.

For the CTA images in the reference segments, default thresholds were used (Table II). For the CTA images in the stenotic segment of patient 2, the average intensity in the center of the image was used as high threshold value and again a default low-threshold value. For the 3DRA images,

for which the intensity scale is not standardized, all thresholds were derived from the images. For each image, the minimum and maximum pixel values were determined and the image was thresholded with the mean value of these two. Next, a refined threshold was determined as the average of the mean foreground and mean background of the initial segmentation, the image was again segmented, and new average foreground and background intensities were determined (I_{fgr} and I_{bgr}). The threshold values were derived from these intensities (Table II).

For the 3DRA images in the stenotic segment, the high threshold was obtained in the same way as for the CTA images in this segment.

For the images in the stenotic segment of patient 1 (containing calcifications), the following procedure was used: The pixels of the central artery and calcifications, if present, were identified by thresholding with the low-threshold value. Next, the pixels of calcifications were identified by thresholding the initial image with a higher threshold. For this threshold, $I_f + 25$ HU was chosen, with I_f as the mean value within the lumen of the reference segments. In order to obtain a better initialization at the proximal and distal edge of the calcification, where the intensity of the calcification is lower because of the partial volume effect, the 3D image with calcification pixels was dilated 0.8 mm (8 pixels) in the z -direction. The structure consisting of the remaining pixels in the thresholded image was used as initialization of the artery, after a morphological opening⁴⁷ of this structure (three times with a 3×3 mask), in order to remove remaining thin strips of pixels at the border of the calcification.

IV.B.2. Definition ROI

In each image, a ROI was defined as the initial segmentation of the central artery with an added border region. Thus, only the part of the calcification or other high-intensity structures within the border region was used in the model fitting. For the images of the reference segments, a width of the border region of 1 mm (10 pixels) turned out to be adequate. For the images of the stenotic segments, a border with a width of 1.5 mm (15 pixels) was chosen in order to

TABLE III. Average estimated values of the diameter $D=2R$, σ , I_f , and I_b and their standard deviations using the cylindrical model with six parameters. The values of \hat{I}_f and \hat{I}_b in the two phantoms are slightly different. Av.: Average; SD: Standard deviation.

Phantom	D (mm)	No. of images	\hat{D} (mm)		$\hat{\sigma}$ (mm)		\hat{I}_f (HU)		\hat{I}_b (HU)		No. of restarts	
			Av.	SD	Av.	SD	Av.	SD	Av.	SD	Av.	Range
1	6.0	173	6.01	0.046	0.406	0.014	335	2	82	2	1.3	1–3
2	4.0	164	4.06	0.031	0.407	0.011	359	2	87	1	1.3	1–3
2	2.8	41	2.80	0.042	0.411	0.017	365	6	86	2	1.8	1–8
1	2.4	46	2.43	0.037	0.416	0.019	346	8	78	2	1.5	1–4
2	1.6	47	1.65	0.094	0.416	0.031	365	35	84	1	2.1	1–8
1	1.2	46	1.16	0.210	0.422	0.049	421	185	77	1	3.8	1–9
2	0.8	39	0.82	0.252	0.395	0.051	410	159	85	2	5.4	1–22
1	0.6	41	0.67	0.215	0.424	0.065	412	128	78	2	4.7	1–11
2	0.4	36	0.43	0.086	0.439	0.101	390	41	86	1	3.1	1–12

include more extraneous structures that might affect the modeling of the central artery. To the initial segmentation of the ROIs of the CTA images isolated regions were added with an intensity between 100 and 150 HU, determined by thresholding, which were used as additional structures in the fitting process. This last step was performed to improve the quality of the fit for some of the images in which the central carotid artery had a low contrast.

IV.B.3. Initialization of p and dp

Initial values for x_0 , y_0 , I_f , and σ were chosen as described for the phantom images in Sec. IV A. For the CTA images a default value $I_b=50$ HU was used; for the 3DRA images $I_b=I_{bgr}$ was used (Sec. IV B 1). Initial values of the Fourier parameters were obtained as follows.

The contour surrounding each shape was sampled at $M=64$ points by intersecting the contour with M lines drawn radially from an initial center point (x_0, y_0) at M angles uniformly distributed in $[0, 2\pi)$. The resulting curve can be described as $\{x(t_j), y(t_j)\}$, with $t_j=2\pi j/M, j=0, 1, M-1$, and the initial EFD parameters were computed as³⁰

$$\begin{aligned} x_0 &= \frac{1}{M} \sum_{j=0}^{M-1} x(t_j), & y_0 &= \frac{1}{M} \sum_{j=0}^{M-1} y(t_j), \\ a_k &= \frac{2}{M} \sum_{j=0}^{M-1} x(t_j) \cos(kt_j), & b_k &= \frac{2}{M} \sum_{j=0}^{M-1} x(t_j) \sin(kt_j), \\ c_k &= \frac{2}{M} \sum_{j=0}^{M-1} y(t_j) \cos(kt_j), & d_k &= \frac{2}{M} \sum_{j=0}^{M-1} y(t_j) \sin(kt_j). \end{aligned} \quad (6)$$

The effect of the choice of the number N of Fourier terms was studied. It appeared that the cross-sections of the carotid arteries in the reference images could be best described with $N=4$ and in the stenotic segments with $N=1$, i.e., as ellipses. Motivations for this choice and more details are given in Sec. V.

Initial values for dx_0 , dy_0 , dI_f , dI_b , and $d\sigma$ were chosen as for the phantom images (Table I). The following initial values for the Fourier terms were used: da_k was chosen as $0.2a_k$ or 1 pixel, whatever was greater, db_k , dc_k , and dd_k likewise.

For the images of the reference segments, all model images were fitted using all parameters of the extended model. For the CTA images of the stenotic segments, model images were fitted with all parameters and also with a restricted set of parameters, using for I_f , I_b , and σ the mean estimates of these parameters for the relevant reference segments as prior knowledge. For the 3DRA images of the stenotic segments, no prior knowledge was used because I_f may vary substantially within a few cm because of the arterial injection of the contrast agent.

IV.B.4. Calculation of model images and minimization of the objective function

Images of the extended model were calculated as described in Sec. II C.

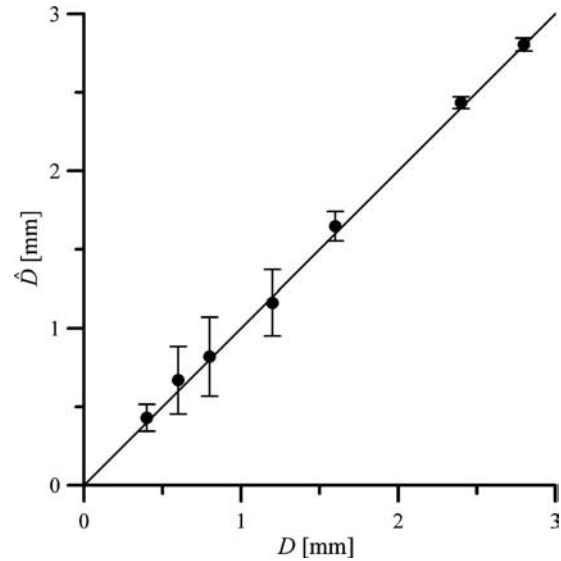


FIG. 3. Average estimated values of the diameter $\hat{D} \pm 1$ standard deviation using the cylindrical model with six parameters. The line of identity is also shown. In order to facilitate comparison with Fig. 5, measurements up to 3 mm are shown. Estimated values for 4 and 6 mm can be found in Table III.

In the (unblurred) model image with a central artery and an adjoining calcification, sometimes an overlap between arterial lumen and calcification occurred. In case of overlap, the pixels in the model image (before blurring) were set to the highest value, i.e., to the intensity of the calcification, and the area of the artery was taken as the area of the arterial shape minus the area of the overlapping region.

Because of the separability of the Gaussian kernel used in the blurring of the images, the 2D convolution could be performed by two successive convolutions with a 1D Gaussian kernel in the x - and y -directions. These kernels were truncated at 3σ from the center.

In the simplex algorithm, again, a maximum of 500 iterations was chosen. Convergence was generally slower than for the phantom images. If after 15 restarts no convergence had been reached, the minimization procedure was terminated and the last parameter estimates were used.

V. RESULTS

V.A. Phantom data

The estimated diameters (\hat{D}) using the cylindrical model with all six parameters are shown in Fig. 3 and in Table III. Although the accuracy of the diameter estimates is satisfactory, the standard deviation (SD) for diameters less than 1.5 mm increases sharply. This increase in SD is also present for σ and I_f . This is caused by the fact that for small diameters, only two of the three parameters D , I_f , and σ are independent, where we have taken for simplicity I_b to be constant. Thus unambiguous estimation of all three parameters is not possible and the use of prior knowledge of at least one of these parameters is mandatory.²⁷ This dependency appears from the high correlation between D , I_f , and σ in this range

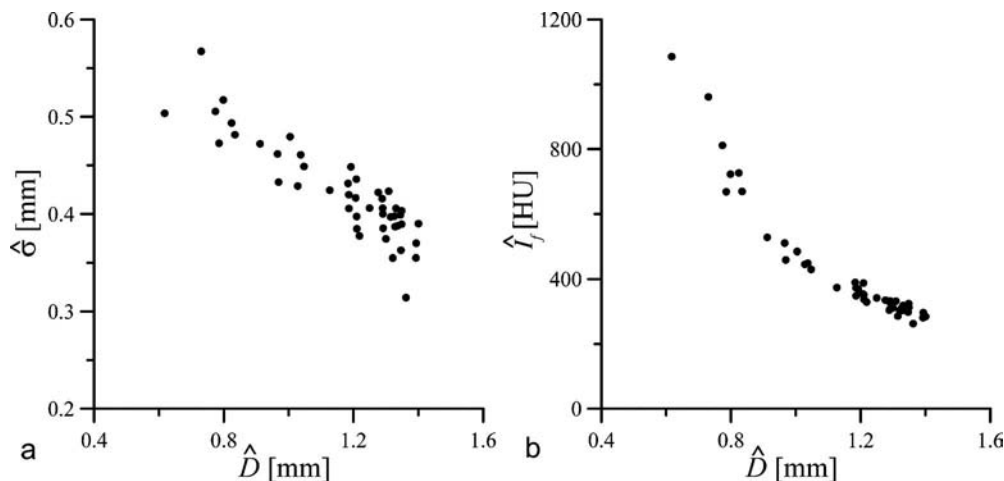


FIG. 4. Relation between estimated values of (a) the diameter (\hat{D}) and sigma ($\hat{\sigma}$) and (b) the diameter (\hat{D}) and the intensity (\hat{I}_p) of the cylindrical hole with a diameter of 1.2 mm.

(see Fig. 4 for an example) and the large number of restarts that is needed to obtain convergence (Table III).

The estimated diameters using three free parameters (x_0 , y_0 , and R) and fixed values for I_f , I_b , and σ are shown in Fig. 5 and in Table IV. Here both the accuracy and precision are satisfactory.

Figure 5 also displays the diameter estimates according to the FWHM criterion and the estimates based on the second order derivative zero-crossing, calculated using Eq. (3). This figure demonstrates the range of diameters for which these methods lead to a bias (for $\sigma=0.4$, the value of the phantom study).

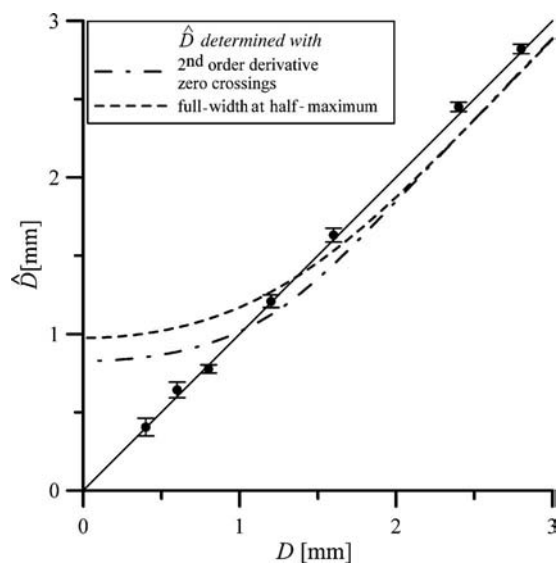


FIG. 5. Average estimated values of the diameter $\hat{D} \pm 1$ standard deviation, using the three-parameter cylindrical model, in which prior knowledge of I_f , I_b , and σ is used. The upper curve shows the diameters when the full-width at half-maximum criterion is used, the lower curve displays the diameters as determined using second derivative zero-order crossing. The line of identity is also shown.

V.B. PSF measurements

The value of σ measured in the scan of the PVC cube was 0.414 mm (SD 0.012 mm). This value is nearly the same as the most precise estimates of σ obtained from the phantom data with the cylindrical model (0.41 mm; Table III).

V.C. Patient data

Figure 6 shows the registered surfaces of the carotid arteries of both patients. The reference segments and stenosed segments are indicated.

V.C.1. Reference segments

The cross-section of the carotid artery of patient 1 was somewhat elongated in the proximal segment, while in the distal reference segment and in both reference segments of patient 2, it was reasonably circular. A typical example of a noncircular carotid cross-section of patient 1 is shown in Fig. 7: Fig. 7(a) shows the CTA image and Fig. 7(d) the 3DRA

TABLE IV. Average estimated value of the diameter $D=2R$ and standard deviation using the cylindrical model with three free parameters and prior knowledge of I_f , I_b , and σ . The average number of restarts for convergence was between 1.1 and 1.2. Av.: Average; SD: Standard deviation.

Scan	D (mm)	No. of. images	\hat{D} (mm)	
			Av.	SD
2	2.8	41	2.82	0.030
1	2.4	46	2.45	0.030
2	1.6	47	1.63	0.044
1	1.2	46	1.21	0.039
2	0.8	39	0.78	0.026
1	0.6	41	0.64	0.050
2	0.4	36	0.41	0.056

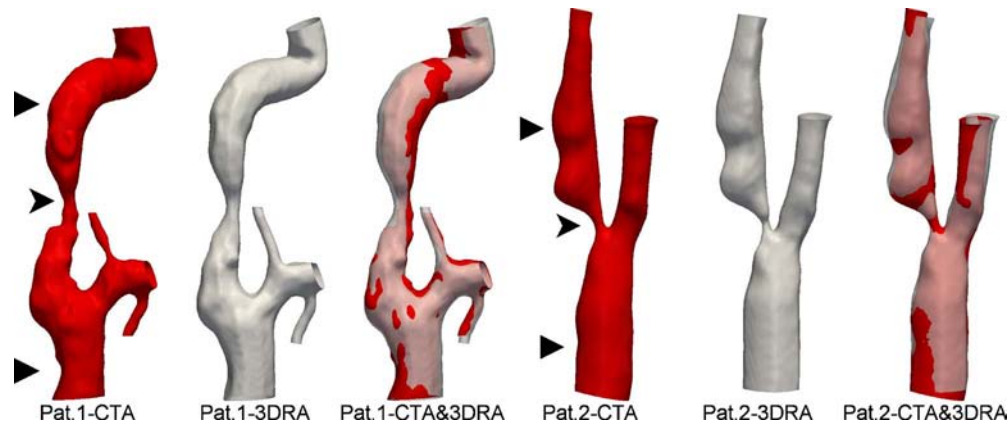


FIG. 6. Registered surfaces of CTA images and 3DRA images of both patients. The centers of the stenotic segment are indicated with an arrow head and the centers of the reference segments are indicated with a triangle.

image. The extended model was fitted using zero, one, two, four, and six Fourier terms, respectively. Fitted model images with four Fourier terms and the contours of the unblurred shapes are shown in Figs. 7(b), 7(c), 7(e), and 7(f). The

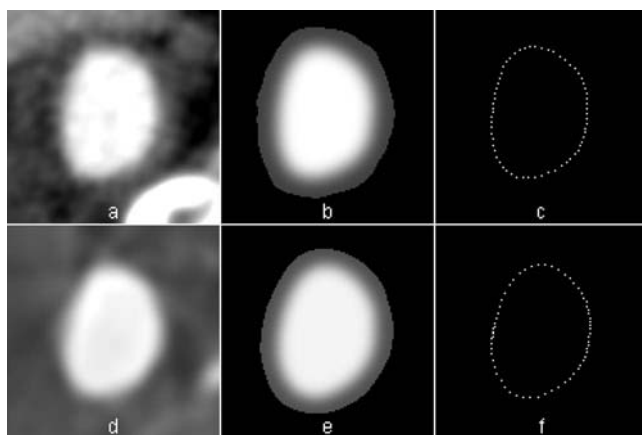


FIG. 7. Cross-sections of the common carotid artery of patient 1, second image of the proximal section (Fig. 9, at 0.5 mm). (a) shows the CTA image and (d) the 3DRA image. The other figures show the fitted model images (middle column) and contours (last column) for CTA (upper) and 3DRA (lower) using four Fourier terms. The contours bound the (unblurred) shapes. Each image measures $12.8 \times 12.8 \text{ mm}^2$. The window center is 160 HU and the window width is 400 HU for images (a) and (b); the window width and level in the images (d) and (e) were chosen to obtain approximately the same gray values for the artery and background.

number of restarts before convergence, RMS error, estimated equivalent diameter \hat{D} , and other parameter values for the CTA image are shown in Table V.

The choice of the number of Fourier terms determines the quality of the fit of the shape: Too few terms may produce a shape that is too simplistic and too many terms may result in an erroneous curve. This last is especially the case for shapes with a smaller equivalent diameter and/or a lower contrast, and in cases of evident mismatch (Fig. 8).

From visual inspection, it appears that for the example in Fig. 7, four Fourier terms are adequate and, because the other cross-sections in the reference segments were more circular than this one, adequate for all reference segments. It is evident that the estimated value of the equivalent diameter is not very sensitive for the number of Fourier terms used; the diameter is virtually constant for $N=2$ and higher. In the example shown in Fig. 7, with four Fourier terms, the estimated equivalent diameter of the 3DRA image is 6.75 mm, virtually the same value as for the CTA image (see Fig. 9).

In the reference images, sometimes high-intensity structures were present in the periphery of the ROI (Fig. 8). These shapes could be adequately described as ellipses ($N=1$). Figure 8 shows the importance of the inclusion of these structures. When only the central shape is fitted, its contour is drawn toward the higher intensity region in the periphery. This results in anomalies, dependent on the number of Fourier terms used.

TABLE V. Details of the fit of a model image to the CTA image of Fig. 7(a). The number of Fourier terms (N) increases from 0 (i.e., a circle) to 6. In Fig. 7(b), a fitted image with $N=4$ is shown. EFD: Elliptical Fourier descriptors; RMS err.: Root mean square error.

N (no. of EFD)	No. of restarts	RMS err. (HU)	\hat{D} (mm)	$\hat{\sigma}$ (mm)	\hat{I}_f (HU)	\hat{I}_b (HU)
0	1	48.9	6.61	0.573	365	78
1	4	21.8	6.85	0.512	360	53
2	14	16.4	6.76	0.478	363	61
4	4	15.7	6.74	0.473	363	62
6	13	14.9	6.73	0.466	363	63

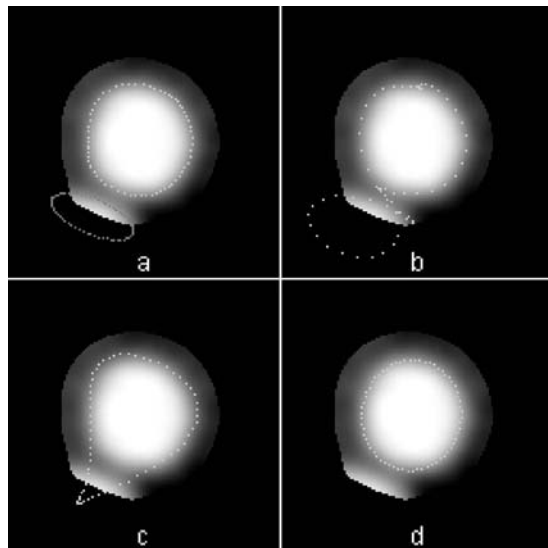


FIG. 8. CTA image of the common carotid of patient 2, ninth image of the distal section (Fig. 10 at 29 mm), with a high-intensity structure in the periphery of the ROI (at the lower left). (a) shows the fitted contours with $N=4$ for the central artery and $N=1$ for the peripheral shape. (b)–(d) show the effect of disregarding the peripheral shape; in (b), the same number of Fourier terms ($N=4$) was used as in (a); in (c) $N=2$ and in (d) $N=1$. Each image measures 12.8×12.8 mm². The window center is 200 HU; the window width is 500 HU.

Incidentally a large number of restarts were needed for convergence, up to 15, the maximal number used in the present study. Although in this last case no convergence was reached, because the RMS error still decreased, the practical consequences were negligible, as the changes in estimated parameter values (and RMS errors) in the last iterations were very small.

Figures 9 and 10 (left side) show the estimated equivalent diameters for the reference segments for both patients. For patient 1, the agreement between the equivalent diameters

derived from CTA images and 3DRA images is fair to good, with exception of the most distal images. For patient 2, the agreement for the proximal images is good but the differences for the distal images are more pronounced, as the estimated equivalent diameters are systematically higher for the 3DRA images. This may partly be caused by suboptimal registration of the more distal CTA and 3DRA images (Sec. III D 3), but is mainly due to severe artifacts that show up in a large number of the 3DRA images. These artifacts consist of large variations in the intensity of the surrounding of the artery and this results in poor fits of the model images to the 3DRA images (see Fig. 11). For the CTA images, the intensities within and outside the artery, \hat{I}_f and \hat{I}_b , and blurring parameters $\hat{\sigma}$, are reasonably constant in the proximal and distal reference segments. This is evident from the relative low values of the SD which is determined from the collection of measurements at the proximal and distal reference segment (Table VI).

V.C.2. Segments with stenosis

In the stenosed segment of patient 1, calcifications were present (Figs. 12 and 13). In patient 2, the stenosed segment was immediately above the carotid bifurcation (Fig. 6) and in the images of the first part of this segment, a part of the external carotid was within the ROI (Fig. 14).

Because of the smaller dimensions and the lower contrast of the internal carotid arteries in the stenosed segments, a smaller number of Fourier terms N was used for their modeling. This was done because their cross-sectional shape was simpler, because of the smaller dimensions, and to avoid the undesirable anomalies in the shape of the contour we mentioned earlier. For the central artery $N=1$ was used, i.e., an

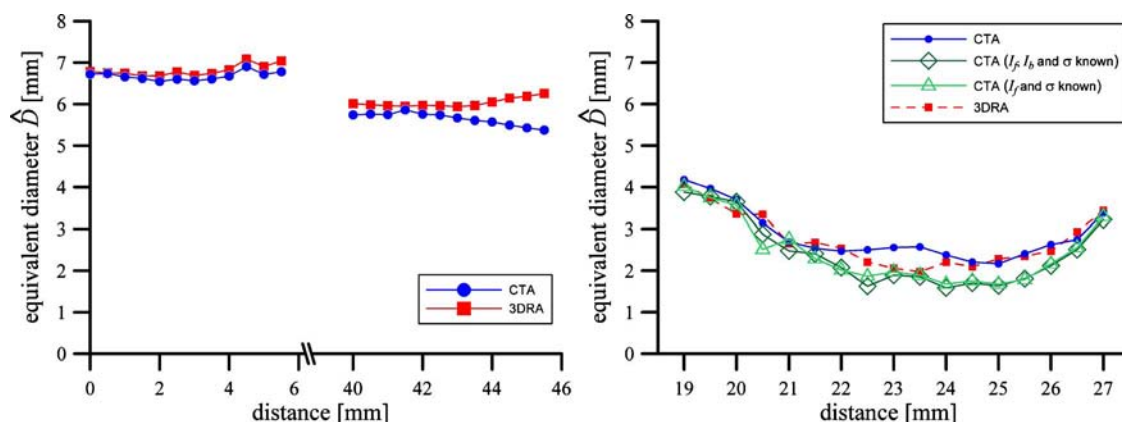


FIG. 9. Estimated equivalent diameters of the carotid of patient 1. On the left are the equivalent diameters of both reference segments. CTA measurements are indicated with circles; 3DRA measurements with squares. On the right are the equivalent diameters of the stenosed segment. For the CTA and 3DRA measurements without use of prior knowledge, the same symbols are used as at left. Rotated squares and triangles indicate CTA measurements with the use of prior knowledge of three and two parameters, respectively (see text). In the reference sections, $N=4$ Fourier terms were used. In the stenosed section, $N=1$ was used for the arteries (i.e., ellipses were fitted) and $N=2$ was used for the calcifications and other peripheral densities, except when they were very small (area < 1 mm²). In the last case, $N=1$ was used. At the horizontal axis, the distance of the first proximal cross-section is indicated (in mm); at the vertical axis, the equivalent diameter (in mm).

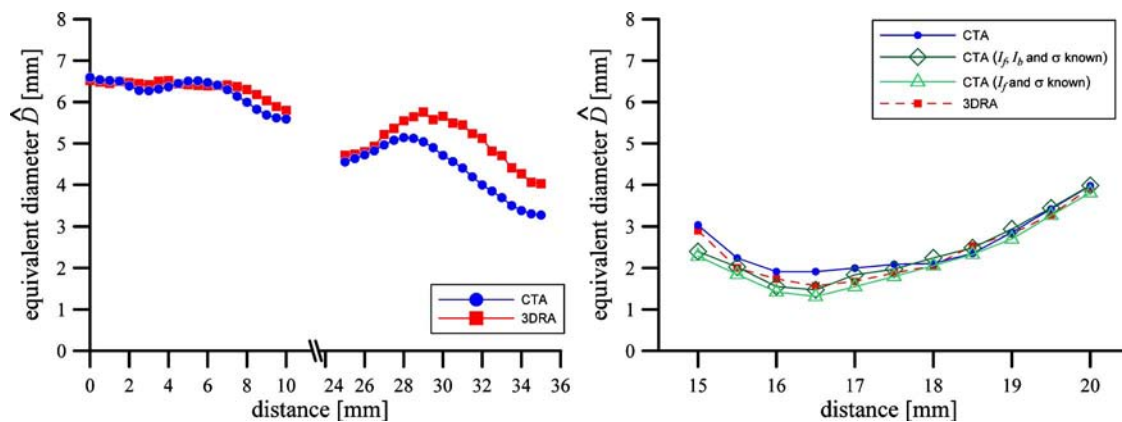


FIG. 10. Estimated equivalent diameters of the carotid artery of patient 2. Details as in Fig. 9.

ellipse was fitted. To model the peripheral high-intensity structures $N=2$ turned out to be adequate, except for very small structures (initial area $<1 \text{ mm}^2$), for which $N=1$ was sufficient.

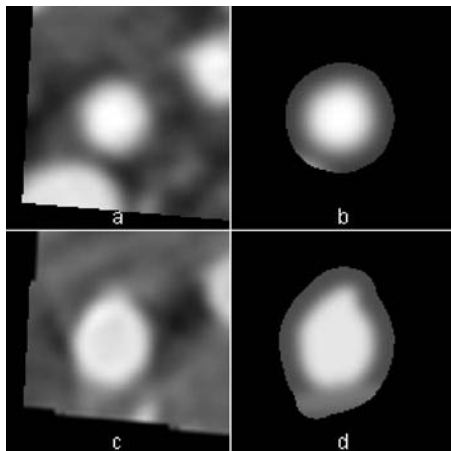


FIG. 11. Cross-sections of the common carotid of patient 2, image 16 of the distal reference segment (Fig. 10, at 32.5 mm) (a) shows the CTA image and (c) the 3DRA image. (b) and (d) show the fitted model images, using four Fourier terms. Note the severe streak artifacts in the 3DRA image (c), with background values varying between -600 and 600 , with the intensity of the artery in the order of 1800 (all arbitrary units) and edge enhancement of the artery. These artifacts, probably in combination with some mismatch, cause deviations in the shape of the artery [see (c) in comparison with (a)] and a poor fit (d). As a consequence, the estimated equivalent diameter in (d) is much larger than that in (b) (see Fig. 10). Each image measures $12.8 \times 12.8 \text{ mm}^2$. The window center is 170 HU and the window width is 600 HU for images (a) and (b); the window width and level in the images (c) and (d) were chosen to obtain approximately the same gray values for the artery and background.

For the images in the stenosed segment frequently a large number of restarts were needed to obtain convergence, up to 15, the maximal number used. It appeared that a larger number of restarts were needed when more shapes were fitted. Like for the reference segments, the consequences for not reaching the strict convergence criterion were negligible, as changes in the estimated equivalent diameters (and RMS errors) in the last iterations were very small.

In Figs. 9 and 10 (right), the estimated equivalent diameters in the stenosed segment are shown. For the CTA measurements, it appears that the equivalent diameters estimated with use of prior knowledge are somewhat smaller than those estimated without this knowledge. For patient 1, no systematic differences exist for estimates using prior knowledge for three parameters (I_f , I_b , and σ) or only two (I_f and σ); for patient 2, equivalent diameters obtained using prior knowledge for two parameters are systematically somewhat lower (0.2 mm on the average). This corresponds with the estimated background intensity I_b that is virtually the same for patient 1 as the prior knowledge intensity, but approximately 30 HU higher than the prior knowledge intensity for patient 2. Therefore, for this last patient, the estimates using prior knowledge of two parameters appear to be the most reliable. For this patient the quality of the fit in the stenotic segment appeared to be slightly better when prior knowledge was used [cf. Figs. 14(b) and 14(c)]. The 3DRA estimates, for which no prior knowledge was used, lie somewhere in between, but can hardly be used as reference values because of the artifacts in the 3DRA images (see Figs. 11 and 13).

TABLE VI. Mean values and standard deviations of \hat{I}_f , \hat{I}_b , and $\hat{\sigma}$ for the reference segments of the CTA images of patients 1 and 2. These data are used as prior information in the segments with a stenosis.

Patient no.	$\hat{\sigma}$ (mm)		\hat{I}_f (HU)		\hat{I}_b (HU)	
	Av.	SD	Av.	SD	Av.	SD
1	0.477	0.018	345	11	52	8
2	0.583	0.035	467	7	10	12

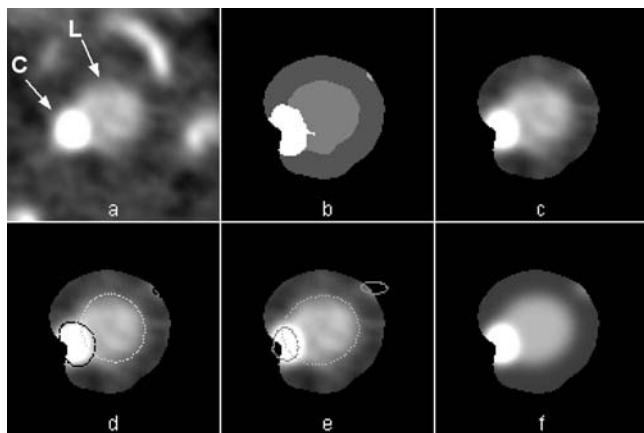


FIG. 12. (a) First CTA image in the proximal part of the stenosed segment of patient 1 with calcification (Fig. 9, at 19 mm); the lumen is indicated with an L and the calcification with a C; (b) ROI with initial segmentation of the artery (light grey), border (dark grey), part of calcification within border (white), and very small part of calcification at top right (light gray); the shape of the calcification in (b) does not correspond exactly with that in (a) because of the 3D dilatation in a preprocessing step (see text); (c) ROI; (d) initialization with $N=1$ (ellipse) for the artery, $N=2$ for the calcification, and $N=1$ for the very small part of the calcification at top right; (e) fitted contours and (f) fitted model images, using prior knowledge of I_f , I_b , and σ . (Table VI, patient 1). Use of prior knowledge of I_f and σ only gave virtually the same fit. The window center is 180 HU and the window width is 500 HU for images (a) and (c)–(f). Each image measures 12.8×12.8 mm²

VI. DISCUSSION

The value of the presented model-based approach for (equivalent) diameter estimation of arteries in CTA images in which prior knowledge is used of essential parameters is evident from phantom measurements. We have shown that this approach can also be applied to the modeling of noncylindrical arteries, with adjacent high-intensity structures, such as calcifications.

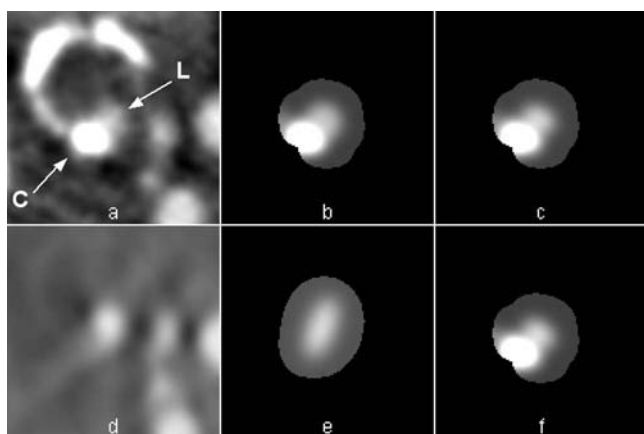


FIG. 13. (a) CTA image at the site of maximal stenosis of patient 1 (Fig. 9, 13th image of stenosis segment at 25 mm); the lumen is indicated with an L and the calcification with a C; (b, c, and f) fitted images using all parameters (b) and prior knowledge of three (c) and two (f) parameters. (d) 3DRA image at the same site with nearly invisible calcification; note the streak artifacts. (e) fitted 3DRA image. Each image measures 12.8×12.8 mm². The window center is 200 HU and the window width is 400 HU for (a)–(c) and (f); for (d) and (e), settings were chosen to obtain approximately the same gray values for artery and background.

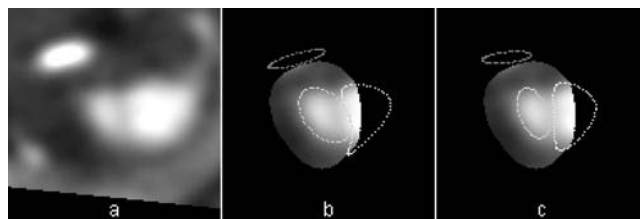


FIG. 14. (a) Cross-section just above the bifurcation of the carotid of patient 2 (first image of the stenosed segment Fig. 10 at 15 mm); [(b) and (c)] ROIs with fitted contours without prior knowledge and with prior knowledge of I_f and σ , respectively (Table VI, patient 2). For the internal and part of the external carotid (middle and right), one and two Fourier terms were used, respectively. Each image measures 12.8×12.8 mm². The window center is 200 HU; the window width is 500 HU.

We first discuss the importance of the use of prior knowledge. Previously, Wörz and Rohr²⁷ demonstrated that when vessels are modeled as blurred cylinders, the use of prior knowledge is indispensable for the estimation of the diameter of *small* vessels. This can be intuitively understood by considering that for a small radius of a blurred cylinder, the intensity distribution $I(r, z_0)$ becomes virtually indistinguishable from a Gaussian. Apart from the location parameters, a Gaussian is described by two parameters, amplitude and σ , and thus of the three parameters of our model R , amplitude $I_f - I_b$, and σ , only two can be independent. For the present study, with $\sigma = 0.4$ mm, this appeared to be the case for diameters in the order of 1.5 mm and less. In the phantom study, it appeared that when prior knowledge was used, accurate and precise diameter estimates could be obtained down to 0.4 mm. For diameters larger than 1.5 mm, the use of prior knowledge was not essential, but still advantageous, as this improved the precision of the estimates.

In the clinical CTA data, the advantage of the use of prior information could not be established unambiguously. Actually this could hardly be expected, as the two patients that were analyzed in this study did not have the narrow vessels (with equivalent diameters ≈ 1.5 mm or less) in which the advantage of prior information is most pronounced.

Of course, the use of prior knowledge is only worthwhile if it is reliable. Therefore, the intensity at the site of the stenosis has to be approximately the same as at the reference site and the border between the artery and surrounding tissue must have a blurring that is adequately described by the PSF determined at the reference site. For the CTA images of this study, both conditions appear to be met. The average intensity before and after stenosis was nearly the same and there is no reason to suspect that at the stenosis site the intensity was different. The blurring parameter σ in the xy -plane can be expected to be constant within the limited field of view that was used in this study and the part of the carotid artery that was analyzed was nearly orthogonal to the xy -plane (Fig. 6). The intensity of the background can be used as prior information as well, but its invariance along the carotid cannot always be guaranteed. In one patient the background intensity was indeed constant, but in the other patient the background intensity of the reference segment was about 30 HU lower than that of the stenotic segment.

The other important point of this study is the generalization to the modeling of noncylindrical arteries and adjacent high-intensity structures. Model-based studies until now were restricted to vessels with circular cross-sections in homogeneous backgrounds. Both restrictions are often in conflict with reality. Especially diseased vessels have noncircular cross-sections, the more so when calcifications are present. This point is extensively discussed by Bartlett.⁴⁸ Moreover, healthy vessels are, at best, only approximately circular too. Additionally, it is important to estimate the parameters that can be used as prior knowledge accurately and when a circular approximation is used, substantial errors may be made. In the example of Table V, the blurring parameter σ , for example, is overestimated by more than 20% when the circular approximation is used. The assumption of a homogeneous background may also produce considerable errors (see, for example, Fig. 8).

In this study, we used elliptic Fourier descriptors to describe noncircular shapes. Results from two patients show that this approach is feasible and that it performs reasonably well. A choice has to be made of the number of Fourier terms that is used. In the two patients in the present study, the nonstenosed carotids could be adequately described with four terms. It is interesting to note that although the use of a higher number of terms was important for an adequate description of the artery cross-section and the accurate estimation of the parameters that were used as prior information, the choice of the number of terms influenced the values of the estimated equivalent diameters only in a minor degree. This is not surprising, given that the equivalent diameter is derived from the cross-sectional area and provides an estimate of the diameter of an equivalent cylindrical vessel. Within the stenosed segments, with smaller arteries and less contrast, fewer terms were used because under these conditions, the use of too many Fourier terms could result in oscillating contours. Although most high frequencies disappeared in the final image because of the smoothing applied, oscillating contours are most likely not in correspondence with the real situation in the body.

The accuracy of the equivalent diameter estimates in the clinical images could not be established unambiguously because no gold standard of high accuracy was present. It was our intention to validate these measurements with equivalent diameter estimates using matched 3DRA images. As the signal-to-noise ratio of the carotids is much higher in 3DRA images than in CTA images and calcifications are virtually invisible in 3DRA images, we expected more precise and more accurate measurements in 3DRA images. However, the quality of these images was often impaired by the presence of severe artifacts, which showed up as shading in the background, and/or inhomogeneities in the enhancement within the arteries. In view of the impaired quality of some of the 3DRA images, the agreement of the equivalent diameters of the stenosed segments measured in the CTA images and 3DRA images is promising. In future studies the quality of 3DRA images could possibly be improved, for instance by incorporating a better beam hardening correction and ECG

gating. In that case, 3DRA could be a more useful standard for the judgment of the performance of the present method in CTA images.

In the present study, the size of the arterial lumen was characterized with the equivalent diameter, derived from the cross-sectional area. A more sophisticated postprocessing approach could be taken, if desired, that would select the narrowest projected diameter from the actual modeled boundary. This would more closely mimic the approach taken by NASCET investigators.^{3,48}

The presented method is not yet ready for clinical adaptation. It is, however, an important step in that direction. We discuss some limitations. As mentioned above, the part of the carotid artery that was analyzed was approximately orthogonal to the xy -plane and therefore the blurring can be adequately described by one parameter $\sigma (= \sigma_{xy})$. This is no longer the case when the artery is not orthogonal to the xy -plane and the out-of-plane blurring parameter σ_z differs from σ_{xy} . However, in this case, the blurring can be made isotropic by preblurring in-plane or out-of-plane before the analysis is carried out.^{20,24}

An additional limitation is that the method presented in this article is essentially two-dimensional. In our modeling approach it was assumed that the diameter of the artery changes slowly in the longitudinal (z) direction. This assumption is reasonable for an unobstructed carotid artery and is frequently made (implicitly) in studies on this topic.^{24,26,27} However, when calcifications are present, this need not be the case. A next step should be the implementation of a similar method in 3D, in which 3D parametric shapes are fitted to a volume of interest containing the artery. The problem of abrupt diameter changes when calcifications are present should be alleviated when a 3D method is used. Moreover, the signal-to-noise ratio would effectively increase because the information of a number of neighboring images would be combined in the fitting procedure.

In conclusion, this study stresses the importance to use prior knowledge when the diameter of narrow blood vessels is estimated with a model-based method, and presents a new approach to obtain realistic modeling of blood vessels in patient data.

APPENDIX A: DERIVATION OF EQUATION (3)

We model the carotid artery as a tube with a circular cross-section with a radius that changes slowly in the z -direction, filled with a material with an attenuation coefficient I_f . The tube, with attenuation coefficient I_b , is embedded in a homogeneous surrounding with the same attenuation coefficient. In polar coordinates, the attenuation coefficient distribution is given by

$$\mu(r, \varphi, z) = \mu(r, z) = \begin{cases} I_f & r \leq R(z) \\ I_b & r > R(z) \end{cases} \quad (\text{A1})$$

with $I_f = I_b + \Delta I$. The convolution Eq. (1) with a 3D Gaussian function in polar coordinates is given as

$$\begin{aligned}
I(r, \varphi, z) &= \frac{1}{(2\pi)^{3/2} \sigma_{xy}^2 \sigma_z} \int_0^\infty dr' \int_0^{2\pi} d\varphi' \\
&\times \int_{-\infty}^\infty dz' r' e^{-(r'^2 + r^2)/2\sigma_{xy}^2} \\
&\times e^{rr' \cos(\varphi - \varphi')/\sigma_{xy}^2} e^{-(z - z')^2/2\sigma_z^2} \mu(r', z'). \quad (\text{A2})
\end{aligned}$$

Since μ is independent of φ , the integral is separable in φ such that we can use

$$\int_0^{2\pi} d\varphi e^{rr' \cos(\varphi)/\sigma_{xy}^2} = 2\pi I_0\left(\frac{rr'}{\sigma_{xy}^2}\right), \quad (\text{A3})$$

with I_0 as the modified Bessel function of the first kind and order 0. The Bessel function can be expressed in a series representation

$$I_0(\infty) = \sum_{k=0}^{\infty} \frac{\alpha^{2k}}{(2^k k!)^2}, \quad (\text{A4})$$

such that Eq. (A3) can be written as

$$\begin{aligned}
I(r, z) &= \frac{1}{\sqrt{2\pi} \sigma_{xy}^2 \sigma_z} \sum_{k=0}^{\infty} \frac{1}{(2^k k!)^2} \int_0^\infty dr' \int_{-\infty}^\infty dz' r' \\
&\times \left(\frac{rr'}{\sigma_{xy}^2}\right)^{2k} e^{-(r'^2 + r^2)/2\sigma_{xy}^2} e^{-(z - z')^2/2\sigma_z^2} \mu(r', z'). \quad (\text{A5})
\end{aligned}$$

When we assume that the radius R is slowly varying on the scale σ_z , the z -component of the 3D Gaussian PSF approximates a delta function such that we can use the following approximation:

$$\frac{1}{\sqrt{2\pi} \sigma_z} \int_{-\infty}^\infty dz' e^{-(z - z')^2/2\sigma_z^2} \mu(r', z') \approx \mu(r', z), \quad (\text{A6})$$

Using Eqs. (A6) and (A1), Eq. (A5) leads to

$$I(r, z) = I_b + \frac{\Delta I}{\sigma_{xy}^2} \sum_{k=0}^{\infty} \frac{1}{(2^k k!)^2} \int_0^{R(z)} dr' r' \left(\frac{rr'}{\sigma_{xy}^2}\right)^{2k} e^{-(r'^2 + r^2)/2\sigma_{xy}^2} \quad (\text{A7})$$

By factoring out all terms independent from r' , Eq. (A7) is given by

$$\begin{aligned}
I(r, z) &= I_b + \frac{\Delta I}{\sigma_{xy}^2} e^{-r^2/2\sigma_{xy}^2} \sum_{k=0}^{\infty} \frac{1}{(2^k k!)^2} \left(\frac{r}{\sigma_{xy}^2}\right)^{2k} \\
&\times \int_0^{R(z)} dr' r'^{2k+1} e^{-r'^2/2\sigma_{xy}^2}. \quad (\text{A8})
\end{aligned}$$

The integration over r' can be solved using

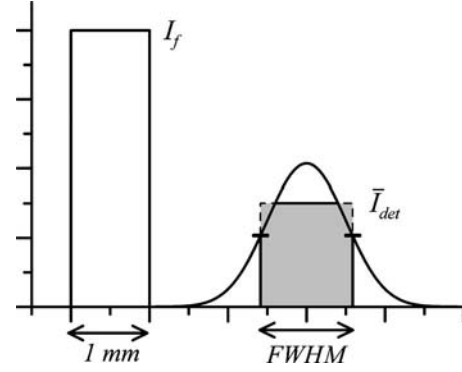


FIG. 15. Cross-sections of the 2D intensity profiles of a disk-shaped detail with a diameter of 1 mm and intensity I_f (left) and of the same detail blurred with a Gaussian PSF with a σ of 0.4 mm (right). The integrated intensity of the unblurred detail is the same as that of the blurred detail. \bar{I}_{det} is the mean intensity within the FWHM. In this example, $I_b = 0$. The integrated intensity of the blurred detail can be approximated with the integrated intensity within the FWHM multiplied by a factor $f > 1$ to allow for the tails that are not included in the integration. For a Gaussian profile, which is a good approximation to the true intensity distribution in this example, $f = 2$.

$$\begin{aligned}
\int_0^{R(z)} dr' r'^{2k+1} e^{-r'^2/2\sigma_{xy}^2} &= \left| -2^k \sigma_{xy}^{2k+2} \Gamma\left(1 + k, \frac{r'^2}{2\sigma_{xy}^2}\right) \right|_0^{R(z)} \\
&= 2^k \sigma_{xy}^{2k+2} \left(k! - \Gamma\left(1 + k, \frac{R(z)^2}{2\sigma_{xy}^2}\right) \right), \quad (\text{A9})
\end{aligned}$$

with $\Gamma(a, x)$ as the incomplete gamma function. This leads to our final representation.

$$\begin{aligned}
I(r, z) &= I_b + (I_f - I_b) e^{-r^2/2\sigma_{xy}^2} \sum_{k=0}^{\infty} \frac{1}{k!^2} \left(\frac{r^2}{2\sigma_{xy}^2}\right)^k \\
&\times \left(k! - \Gamma\left(1 + k, \frac{R(z)^2}{2\sigma_{xy}^2}\right) \right). \quad (\text{A10})
\end{aligned}$$

APPENDIX B: INITIAL VALUE OF THE EQUIVALENT DIAMETER FOR SMALL VESSELS

The initial value for the equivalent diameter or radius of small vessels (diameter 1 mm or less) was obtained by using the property that the integrated intensity Π_{blurred} of a blurred detail is the same as the integrated intensity Π_{sharp} of the unblurred detail, both relative to the background. We first discuss the continuous situation (see Fig. 15).

For a disk-shaped detail,

$$\Pi_{\text{sharp}} = \pi R^2 (I_f - I_b), \quad (\text{B1})$$

with R as the radius of the disk and I_f and I_b as the intensity of disk and background.

To avoid problems with the integration of the intensity of the blurred detail that will be encountered in practice, because of the (in principle) infinite integration limits and the presence of noise, we calculate Π_{blurred} as the integral within the FWHM, multiplied by a factor f to allow for the tails that are not included in the integration

$$\Pi_{\text{blurred}} = f \cdot \pi R_{\text{HM}}^2 (\bar{I}_{\text{det}} - I_b), \quad (\text{B2})$$

with $R_{\text{HM}} = \text{FWHM}/2$ and \bar{I}_{det} as the mean intensity within the FWHM. For a Gaussian profile, $f=2$, and this value is also a good approximation for blurred disks with a diameter of 1 mm or less (for $\sigma=0.4$ mm).

In the discrete situation we start with an initial segmentation of vessel cross-section and background, obtained by thresholding at half of the maximal value of the vessel cross-section relative to the background. The area of the vessel cross-section is S_{vessel} , its mean intensity \bar{I}_{vessel} , and the mean intensity of the background \bar{I}_{bg} . Then

$$\Pi_{\text{measured}} = f \cdot S_{\text{vessel}} (\bar{I}_{\text{vessel}} - \bar{I}_{\text{bg}}). \quad (\text{B3})$$

Because $\Pi_{\text{measured}} \cong \Pi_{\text{blurred}} = \Pi_{\text{sharp}}$, we can initialize the equivalent radius R with

$$R_{\text{ini}} \cong \sqrt{\frac{f \cdot S_{\text{vessel}} (\bar{I}_{\text{vessel}} - \bar{I}_{\text{bg}})}{\pi(I_f - I_b)}}, \quad (\text{B4})$$

with $f=2$. For $(I_f - I_b)$ a default value was used, see the main text.

We finally note that initialization Eq. (B4) can be used for small cross-sections of arbitrary shape as well. In the two patients analyzed in this study these small cross-sections did not occur, however.

^{a)}Electronic mail: hugo@milabs.com

- ¹Executive Committee for the Asymptomatic Carotid Atherosclerosis Study, "Endarterectomy for asymptomatic carotid artery stenosis," *JAMA* **273**(18), 1421–1428 (1995).
- ²European Carotid Surgery Trialists' Collaborative Group, "Randomised trial of endarterectomy for recently symptomatic carotid stenosis: Final results of the MRC European Carotid Surgery Trial (ECST)," *Lancet* **351**(9113), 1379–1387 (1998).
- ³H. J. Barnett et al., "Benefit of carotid endarterectomy in patients with symptomatic moderate or severe stenosis," *N. Engl. J. Med.* **339**(20), 1415–1425 (1998).
- ⁴"Prevention of disabling and fatal strokes by successful carotid endarterectomy in patients without recent neurological symptoms: Randomised controlled trial," *Lancet* **363**(9420), 1491–1502 (2004).
- ⁵S. M. Debrey, H. Yu, J. K. Lynch, K. O. Lovblad, V. L. Wright, S. J. Janket, and A. E. Baird, "Diagnostic accuracy of magnetic resonance angiography for internal carotid artery disease: A systematic review and meta-analysis," *Stroke* **39**(8), 2237–2248 (2008).
- ⁶M. J. Koelmay, P. J. Nederkoorn, J. B. Reitsma, and C. B. Majoie, "Systematic review of computed tomographic angiography for assessment of carotid artery disease," *Stroke* **35**(10), 2306–2312 (2004).
- ⁷I. Kane, W. N. Whiteley, P. A. Sandercock, and J. M. Wardlaw, "Availability of CT and MR for assessing patients with acute stroke," *Cerebrovasc. Dis.* **25**(4), 375–377 (2008).
- ⁸C. L. Siström and N. L. McKay, "Costs, charges, and revenues for hospital diagnostic imaging procedures: Differences by modality and hospital characteristics," *J. Am. Coll. Radiol.* **2**(6), 511–519 (2005).
- ⁹H. Scherl, J. Hornegger, M. Prummer, and M. Lell, "Semi-automatic level-set based segmentation and stenosis quantification of the internal carotid artery in 3D CTA data sets," *Med. Image Anal.* **11**(1), 21–34 (2007).
- ¹⁰S. Suzuki, S. Furui, T. Kaminaga, and T. Yamauchi, "Measurement of vascular diameter in vitro by automated software for CT angiography: Effects of inner diameter, density of contrast medium, and convolution kernel," *AJR, Am. J. Roentgenol.* **182**(5), 1313–1317 (2004).
- ¹¹S. Suzuki, S. Furui, and T. Kaminaga, "Accuracy of automated CT angiography measurement of vascular diameter in phantoms: Effect of size of display field of view, density of contrast medium, and wall thickness," *AJR, Am. J. Roentgenol.* **184**(6), 1940–1944 (2005).
- ¹²H. M. Silvennoinen, S. Ikonen, L. Soinne, M. Railo, and L. Valanne, "CT angiographic analysis of carotid artery stenosis: Comparison of manual assessment, semiautomatic vessel analysis, and digital subtraction angiography," *AJNR Am. J. Neuroradiol.* **28**(1), 97–103 (2007).
- ¹³Z. Zhang, M. H. Berg, A. E. Ikonen, R. L. Vanninen, and H. I. Manninen, "Carotid artery stenosis: Reproducibility of automated 3D CT angiography analysis method," *Eur. Radiol.* **14**(4), 665–672 (2004).
- ¹⁴T. Boskamp, D. Rinck, F. Link, B. Kummerlen, G. Stamm, and P. Mildnerberger, "New vessel analysis tool for morphometric quantification and visualization of vessels in CT and MR imaging data sets," *Radiographics* **24**(1), 287–297 (2004).
- ¹⁵J. Canny, "A computational approach to edge detection," *IEEE Trans. Pattern Anal. Mach. Intell.* **PAMI-8**(6), 679–698 (1986).
- ¹⁶A. F. Frangi, W. J. Niessen, P. J. Nederkoorn, J. Bakker, W. P. Mali, and M. A. Viergever, "Quantitative analysis of vascular morphology from 3D MR angiograms: In vitro and in vivo results," *Magn. Reson. Med.* **45**(2), 311–322 (2001).
- ¹⁷R. Manniesing, B. K. Velthuis, M. S. van Leeuwen, I. C. van der Schaaf, P. J. van Laar, and W. J. Niessen, "Level set based cerebral vasculature segmentation and diameter quantification in CT angiography," *Med. Image Anal.* **10**(2), 200–214 (2006).
- ¹⁸H. Bouma, A. Vilanova, L. J. van Vliet, and F. A. Gerritsen, "Correction for the dislocation of curved surfaces caused by the PSF in 2D and 3D CT images," *IEEE Trans. Pattern Anal. Mach. Intell.* **27**(9), 1501–1507 (2005).
- ¹⁹P. Mendonça, D. Padfield, J. Miller, and M. Turek, "Bias in the localization of curved edges", in Proceedings of the 8th European Conference on Computer Vision (ECCV), Part II, 2004, pp. 554–565.
- ²⁰H. Bouma, J. O. Bescos, A. Vilanova, and F. A. Gerritsen, "Unbiased vessel-diameter quantification based on the FWHM criterion", in Proceedings of SPIE Medical Imaging 2007: Image Processing, 2007, Vol. 6512, pp. 6512N.
- ²¹R. C. Chan, W. C. Karl, and R. S. Lees, "A new model-based technique for enhanced small-vessel measurements in x-ray cine-angiograms," *IEEE Trans. Med. Imaging* **19**(3), 243–255 (2000).
- ²²H. Fujita, K. Doi, L. E. Fencil, and K. G. Chua, "Image feature analysis and computer-aided diagnosis in digital radiography. 2. Computerized determination of vessel sizes in digital subtraction angiography," *Med. Phys.* **14**(4), 549–556 (1987).
- ²³K. R. Hoffmann, D. P. Nazareth, L. Miskolczi, A. Gopal, Z. Wang, S. Rudin, and D. R. Bednarek, "Vessel size measurements in angiograms: A comparison of techniques," *Med. Phys.* **29**(7), 1622–1633 (2002).
- ²⁴S. Wörz and K. Rohr, "Cramer-Rao bounds for estimating the position and width of 3D tubular structures and analysis of thin structures with application to vascular images," *J. Math. Imaging Vision* **30**(2), 167–180 (2008).
- ²⁵G. J. Streekstra, S. D. Strackee, M. Maas, R. ter Wee, and H. W. Venema, "Model-based cartilage thickness measurement in the submillimeter range," *Med. Phys.* **34**(9), 3562–3570 (2007).
- ²⁶S. Wörz and K. Rohr, "Segmentation and quantification of human vessels using a 3-D cylindrical intensity model," *IEEE Trans. Image Process.* **16**(8), 1994–2004 (2007).
- ²⁷S. Wörz and K. Rohr, "A new 3D parametric intensity model for accurate segmentation and quantification of human vessels," in Proceedings of the 7th International Conference on Medical Image Computing and Computer-Assisted Intervention (MICCAI), 2004, Vol. 3216, pp. 491–499.
- ²⁸F. P. Kuhl and C. R. Giardina, "Elliptic Fourier features of a closed contour," *Comput. Graph. Image Process.* **18**, 236–258 (1982).
- ²⁹L. H. Staib and J. S. Duncan, "Deformable Fourier models for surface finding in 3D images," in Proceedings of SPIE Visualization in Biomedical Computing Conference, 1992, Vol. 1808, pp. 90–104.
- ³⁰Y. Jeong and R. J. Radke, "Reslicing axially-sampled 3D shapes using elliptic Fourier descriptors," *Med. Image Anal.* **11**(2), 197–206 (2007).
- ³¹C. de Monye, F. Cademartiri, T. T. de Weert, D. A. Siepmann, D. W. Dippel, and A. van Der Lugt, "Sixteen-detector row CT angiography of carotid arteries: Comparison of different volumes of contrast material with and without a bolus chaser," *Radiology* **237**(2), 555–562 (2005).
- ³²C. de Monye, T. T. de Weert, W. Zaalberg, F. Cademartiri, D. A. Siepmann, D. W. Dippel, and A. van der Lugt, "Optimization of CT angiography of the carotid artery with a 16-MDCT scanner: Craniocaudal scan direction reduces contrast material-related perivascular artifacts," *AJR, Am. J.*

- Roentgenol. **186**(6), 1737–1745 (2006).
- ³³N. Takeyama *et al.*, “Comparison of 40 and 60 milliliters of contrast in assessment of the carotid artery by computed tomography angiography,” *Acta Radiol.* **49**(9), 1068–1078 (2008).
- ³⁴N. Anzalone *et al.*, “Carotid artery stenosis: Intraindividual correlations of 3D time-of-flight MR angiography, contrast-enhanced MR angiography, conventional DSA, and rotational angiography for detection and grading,” *Radiology* **236**(1), 204–213 (2005).
- ³⁵D. E. Hyde, A. J. Fox, I. Gulka, P. Kalapos, D. H. Lee, D. M. Pelz, and D. W. Holdsworth, “Internal carotid artery stenosis measurement: Comparison of 3D computed rotational angiography and conventional digital subtraction angiography,” *Stroke* **35**(12), 2776–2781 (2004).
- ³⁶W. W. Zhang, L. M. Harris, and M. L. Dryjski, “Should conventional angiography be the gold standard for carotid stenosis?,” *J. Endovasc. Ther.* **13**(6), 723–728 (2006).
- ³⁷S. Schaller, J. E. Wildberger, R. Raupach, M. Niethammer, K. Klingenberg-Regn, and T. Flohr, “Spatial domain filtering for fast modification of the tradeoff between image sharpness and pixel noise in computed tomography,” *IEEE Trans. Med. Imaging* **22**(7), 846–853 (2003).
- ³⁸J. Y. Gauvrit, X. Leclerc, M. Vermandel, B. Lubicz, D. Desprez, J. P. Lejeune, J. Rousseau, and J. P. Pruvo, “3D rotational angiography: Use of propeller rotation for the evaluation of intracranial aneurysms,” *AJNR Am. J. Neuroradiol.* **26**(1), 163–165 (2005).
- ³⁹L. Antiga and D. A. Steinman, “The vascular modeling toolkit,” <http://www.vmtk.org>, 2009.
- ⁴⁰L. Antiga, B. Ene-Iordache, and A. Remuzzi, “Computational geometry for patient-specific reconstruction and meshing of blood vessels from MR and CT angiography,” *IEEE Trans. Med. Imaging* **22**(5), 674–684 (2003).
- ⁴¹L. Antiga, M. Piccinelli, L. Botti, B. Ene-Iordache, A. Remuzzi, and D. A. Steinman, “An image-based modeling framework for patient-specific computational hemodynamics,” *Med. Biol. Eng. Comput.* **46**(11), 1097–1112 (2008).
- ⁴²V. Caselles, R. Kimmel, and G. Sapiro, “Geodesic active contours,” *Int. J. Comput. Vis.* **22**(1), 61–79 (1997).
- ⁴³L. Antiga, B. Ene-Iordache, L. Caverni, G. P. Cornalba, and A. Remuzzi, “Geometric reconstruction for computational mesh generation of arterial bifurcations from CT angiography,” *Comput. Med. Imaging Graph.* **26**(4), 227–235 (2002).
- ⁴⁴P. J. Besl and N. D. McKay, “A method for registration of 3-D shapes,” *IEEE Trans. Pattern Anal. Mach. Intell.* **14**(2), 239–256 (1992).
- ⁴⁵J. A. Nelder and R. Mead, “A simplex method for function minimization,” *Comput. J.* **7**(4), 308–313 (1965).
- ⁴⁶W. H. Press, S. A. Teukolsky, W. T. Vetterling, and B. P. Flannery, *Numerical Recipes in C* (Cambridge University, New York, 2002), p. 292.
- ⁴⁷B. Jähne, *Digital Image Processing*, 6th ed. (Springer-Verlag, Heidelberg, 2005).
- ⁴⁸E. S. Bartlett, S. P. Symons, and A. J. Fox, “Correlation of carotid stenosis diameter and cross-sectional areas with CT angiography,” *AJNR Am. J. Neuroradiol.* **27**(3), 638–642 (2006).